

14

Disk–planet interaction and migration

Frederic Masset

SAP, CE-Saclay, France and IA-UNAM, Mexico

Wilhelm Kley

Universität Tübingen, Institut für Astronomie und Astrophysik, Germany

14.1 Introduction

Directly after the discovery of the very first extrasolar planets around main-sequence stars it has become obvious that the new planetary systems differ substantially from our own Solar System. Amongst other properties one distinguishing feature is the close proximity of several planets to their host stars (hot Jupiters). As it is difficult to imagine scenarios to form planets so close to their parent star it is generally assumed that massive, Jupiter-like planets form further away, and then migrate inwards towards the star due to disk–planet tidal interactions. Hence, the mere existence of hot Jupiters can be taken as clear evidence of the occurrence of migration. Interestingly, theoretically the possibility of migrating planets has long been predicted from the early 1980s.

Another observational indication that some migration of planets must have occurred is the existence of planets in mean motion resonances. Due to converging differential migration of two planets both embedded in a protoplanetary disk they can be captured in a low-order mean motion resonance. The most prominent example is the system GJ 876 where the planets have orbital periods of roughly 30 and 60 days.

In this review we focus on the theoretical aspects of the disk–planet interaction which leads to a change in the orbital elements of the planet most notably its semimajor axis. We only treat systems with a single planet and do not consider planetary systems containing multiple planets.

14.2 Type I migration

We consider in this section the tidal interaction between a low-mass protoplanet orbiting a central star within a laminar gaseous Keplerian disk. This planet exerts

a force on any disk fluid element, which produces a wake in the disk. This wake in turn exerts a force on the planet, which leads to a change in the planet’s orbital elements. The purpose of this section is to specify the wake properties and to evaluate its impact on the orbit of the planet.

14.2.1 Evaluation of the tidal torque

The problem of determining the impact of disk interaction on the evolution of the planet orbit amounts to an evaluation of tidal torques. For a sufficiently small planet mass (an upper limit of which will be specified later) one can perform a linear analysis which consists of considering the Fourier decomposition in azimuth of the planet tidal potential ϕ ,

$$\phi(r, \varphi, t) = \sum_{m=0}^{\infty} \phi_m(r) \cos\{m[\varphi - \varphi_p(t)]\}, \quad (14.1)$$

where $\varphi_p = \Omega_p t$ is the azimuth angle of the planet. One is then left to evaluate the torques Γ_m exerted on the disk by the m -folded potential components $\phi_m(r) \cos[m(\varphi - \Omega_p t)]$. In the linear regime, the total torque is then recovered by summing over all m .

We do not reproduce here the expression and the derivation of these torques, which can be found in Goldreich and Tremaine (1979) or Meyer-Vernet and Sicardy (1987). We rather give a few comments on their physical meanings.

An m -folded external forcing potential $\phi_m(r, \varphi)$ which rotates with a pattern frequency Ω_p in a disk with angular velocity profile $\Omega(r)$ triggers a response whenever the potential frequency as seen in the matter frame $\omega = m(\Omega - \Omega_p)$ matches either 0 or $\pm\kappa$ (κ being the epicyclic frequency). The first case corresponds to a corotation frequency (since it implies $\Omega = \Omega_p$, hence fluid elements corotate with the forcing potential) while the second case corresponds to a Lindblad resonance (outer Lindblad resonance for $\omega = \kappa$ and inner Lindblad resonance for $\omega = -\kappa$). The denomination of Lindblad resonance has historical reasons and comes from galactic dynamics (see Binney and Tremaine, 1987).

14.2.1.1 Torque at Lindblad resonances

In a Keplerian disk, the torque exerted on the disk by the external planetary potential is positive at an outer Lindblad resonance, and negative at an inner Lindblad resonance.

The torque value is independent of the physical processes at work in the disk (Meyer-Vernet and Sicardy, 1987). In the simplest case of a non-self-gravitating, pressureless and inviscid disk, the corresponding angular momentum exchange

occurs at the exact location of the Lindblad resonances, and angular momentum accumulates there. To achieve a steady state, some additional physics is required to get rid of the angular momentum deposited at the resonance by the external perturber. Meyer-Vernet and Sicardy (1987) showed that dissipation (provided for example by a simple drag law: $-Qv$, or by a shear or bulk viscosity), pressure effects or self-gravity can help the disk to transfer the angular momentum away from the resonance, thus allowing a steady state and hence a torque value constant in time. Remarkably, the torque value is not altered by the underlying physics, which only modifies the shape and width of the resonant region.

These authors also worked out the case of a satellite “switched on” at $t = 0$ in a disk and found that, after a transient stage as short as $2/(3\Omega_p)$, i.e. one-tenth of an orbit, the torque adopts a constant value as long as the perturbation remains linear. This result may be useful to bear in mind by numericists who perform simulations of embedded planets. Any torque variation that lasts longer than the first orbit cannot be accounted for by the Lindblad torque transients and has to be attributed either to the corotation torque oscillations (due to the libration of material in the co-orbital region, which occurs on a much longer timescale) or to a gradual change in the disk profiles.

14.2.1.2 Differential Lindblad torque

In order to sum up the Lindblad torques at inner and outer resonances, one must know the effective location of these resonances, which slightly differs from their nominal position owing to pressure effects. The nominal location of the Lindblad resonances can be identified with the WKB turning point in the dispersion relation of pressure-supported density waves in a differentially rotating disk, which reads

$$m^2(\Omega - \Omega_p)^2 = \kappa^2 + c_s^2 \left(\frac{m^2}{r^2} + k_r^2 \right), \quad (14.2)$$

where c_s is the sound speed and k_r the radial wavevector.

The effective position of these resonances, which can be found by setting $k_r = 0$ in Equation (14.2), is shifted with respect to the nominal one. In particular, when $m \rightarrow \infty$, Lindblad resonances pile up at locations given by

$$r = r_c \pm \frac{\Omega}{2A} H \quad (14.3)$$

where $A = 1/2 r d\Omega/dr$ is the first Oort constant, instead of at the orbit. These points of accumulation correspond to the minimum distance from corotation at which the flow is supersonic (Goodman and Rafikov, 2001). In the case of a Keplerian disk, they lie at $\pm(2/3)H$ from corotation. This has the important consequence that the high- m torque components ($m \gg r/H$) undergo a sharp cut-off (Artymowicz,

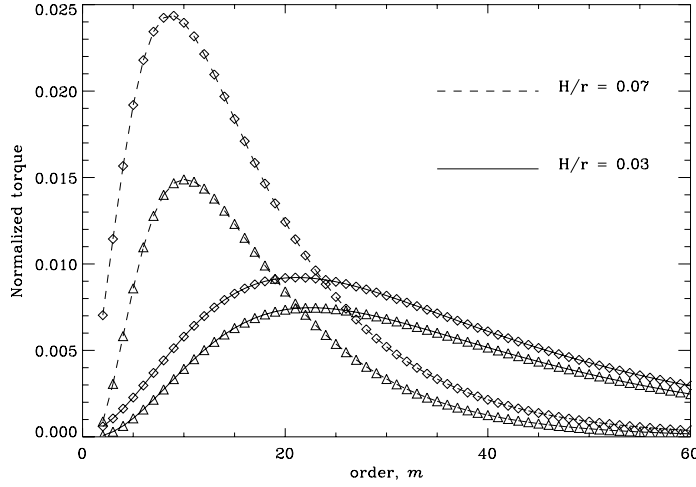


Fig. 14.1. Individual inner and outer torques (in absolute value) in a $h = 0.07$ and $h = 0.03$ disk, as a function of m . For each disk thickness, the upper curve shows the outer torque and the lower one the inner torque. These torques are normalized to $\Gamma_0 = \pi q^2 \Sigma a^4 \Omega_p^2 h^{-3}$. Since one-sided Lindblad torques scale with h^{-3} , the total area under each of the four curves has same order of magnitude.

1993), since high- m potential components are localized in narrow annuli around the perturber orbit, away from the accumulation points, while their width tends to 0 as $m \rightarrow \infty$.

We define the outer (resp. inner) Lindblad torque as the sum of individual Lindblad torques on the outer (resp. inner) Lindblad resonances,

$$\Gamma_{\text{OLR(ILR)}} = \sum_{m=1(2)}^{+\infty} \Gamma_m^{\text{OLR(ILR)}}, \quad (14.4)$$

where the sum begins at $m = 2$ for the inner torque, since an $m = 1$ rotating potential has no ILR in a Keplerian disk. We shall also refer to these torques as one-sided Lindblad torques. They scale with h^{-3} , where $h = H/r$ is the disk aspect ratio (Ward, 1997).

Fig. 14.1 illustrates a number of properties of the one-sided Lindblad torques. In particular, one can see that the torque cut-off occurs at larger m values in the thinner disk (the outer torque value peaks around $m \sim 8 - 9$ for $h = 0.07$, while it peaks around $m \sim 21 - 22$ for $h = 0.03$). Also, there is for both disk aspect ratios a very apparent mismatch between the inner and the outer torques, the former being systematically smaller than the later. If we consider the torque of the disk acting on the planet, then the outer torques are negative and the inner ones positive, and the total torque is therefore negative. As a consequence migration is directed inwards and leads to a decay of the orbit onto the central object (Ward, 1986).

One can note in Fig. 14.1 that the relative mismatch is larger for the thicker disk. Indeed, it can be shown that this relative mismatch scales with the disk thickness (Ward, 1997). Since one-sided torques scale as h^{-3} , the migration rate scales with h^{-2} .

There are several reasons for the torque asymmetry which conspire to make the differential Lindblad torque a sizable fraction of the one-sided torque in a $h = O(10^{-1})$ disk (Ward, 1997). In particular, for a given m value, the inner Lindblad resonance lies further from the orbit than the corresponding outer Lindblad resonance.

14.2.1.3 The pressure buffer

At first glance the negative sign of the differential Lindblad torque might appear as a fragile result. One may think that a steep surface density profile should reverse this torque, as it should strengthen the inner Lindblad torque and weaken the outer one. However, increasing the surface-density gradient (in absolute value) also increases the pressure gradient. The disk rotational equilibrium then implies that the angular-velocity profile drops so that the sum of the centrifugal force and pressure force cancels out the gravitational force from the central object. As a consequence of the smaller disk angular velocity, all resonances are shifted inwards with respect to a shallower surface-density profile case. This effect plays against the aforementioned surface-density weighting of the inner and outer torques. Quantitatively, both effects appear to nearly cancel each other, and migration is always directed inwards for realistic power-law surface-density and temperature profiles. This effect is known as the pressure buffer (Ward, 1997).

14.2.1.4 Torque at a corotation resonance

The angular momentum exchange at a corotation resonance corresponds to different physical processes than at a Lindblad resonance. At the latter the perturbing potential tends to excite epicyclic motion, and, in a protoplanetary disk, the angular momentum deposited is evacuated through pressure-supported waves. Conversely, these waves are evanescent in the corotation region, and are unable to remove the angular momentum brought by the perturber (Goldreich and Tremaine, 1979).

Again, it is instructive to bear in mind a number of properties of the corotation torque exerted on a disk by an m -folded external perturbing potential. This torque scales with the gradient of Σ/B at the corotation radius. Since B is half the flow vorticity, the corotation torque scales with the gradient of (the inverse of) the specific vorticity, sometimes also called the vortensity. The corotation torque

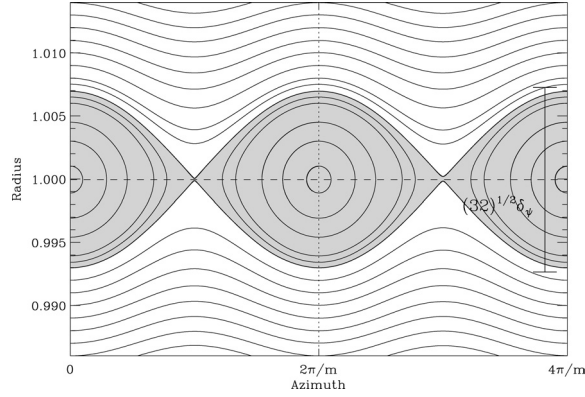


Fig. 14.2. Streamlines in the (φ, r) plane at an $m = 2$ corotation resonance. The gray shaded regions show the libration islands. One can notice that the outer and inner disk streamlines (in the white regions) are circulating, and exhibit radial oscillations with an amplitude that decreases with the distance to the corotation radius ($r = 1$). At the same time they do not show any winding, i.e. all these streamlines reach their maximum distance to the corotation radius at a constant azimuth $\varphi = 0, 2\pi/m, \dots$. This behavior corresponds to the evanescent pressure-supported waves in the corotation region, which have a purely imaginary radial wavevector (no winding and an exponential decay on the disk pressure scalelength).

therefore cancels out in a $\Sigma \propto r^{-3/2}$ disk, such as the minimum-mass Solar Nebula (MMSN).

The physical picture of the flow at a corotation resonance with azimuthal wavenumber m is a set of m eye-shaped libration islands, in which fluid elements librate on closed streamlines. Such islands are depicted in Fig. 14.2. The libration timescale is much larger than the orbital timescale. As a consequence, the motion of librating fluid elements in a non-rotating frame can be considered, on the orbital timescale, as a circular motion. Therefore, these fluid elements carry an amount of specific angular momentum that only depends on their radial position. As they librate, their radial position oscillates about the corotation radius over the libration period, which implies that they periodically give and take back angular momentum from the perturber. As librating fluid elements remain in a radially bounded interval, the angular momentum they exchange with the perturber averages out to zero over a timescale large compared to their libration timescale.

The libration period furthermore depends on the streamline. This implies phase mixing, which makes the corotation torque tend to zero after a few libration timescales, not only on average, but in instantaneous value as well. This is known as the saturation of the corotation torque. It can be avoided if fluid elements have the possibility to exchange angular momentum not only with the perturber, but also

with the rest of the disk. Viscous stress can act to extract angular momentum from the libration islands and prevent saturation.

The corotation-torque saturation can also be described as follows: when the disk viscosity tends to zero, the flow specific vorticity is conserved along a fluid-element path. The libration of fluid elements mixes up the specific vorticity over the libration islands. Once specific vorticity is sufficiently stirred up, an infinitesimally small amount of viscosity suffices to flatten out the specific vorticity over the whole libration island. The corotation torque therefore cancels out, i.e. saturates, since it scales with the vorticity gradient.

In order to avoid saturation, the viscosity must be sufficient to prevent the vorticity profile flattening out across the libration islands. This is possible if the viscous timescale across these islands is smaller than the libration timescale, as shown by Ogilvie and Lubow (2003) and Goldreich and Sari (2003).

Finally, it should be noted that saturation properties are not captured by a linear analysis, since saturation requires a finite libration time, hence a finite resonance width. In the linear limit, the corotation torque appears as a discontinuity at corotation of the advected angular-momentum flux, which corresponds to infinitely narrow, fully unsaturated libration islands.

14.2.2 Corotation torque

All corotation resonances are located at the same corotation radius for a planet in a circular orbit. The flow topology in the co-orbital region of a planet offers striking similarities with the reduced three-body problem of gravitational dynamics. In particular, one can identify a horseshoe region, which is the set of fluid elements librating about the opposite of the planet direction. A sketch of the horseshoe region is given in Fig. 14.3.

Ward (1991, 1992) has identified the full corotation torque with the horseshoe region drag. The physical ingredient that can prevent corotation-torque saturation is viscous stress. In particular, at low ν , the corotation torque is proportional to ν (Balmforth and Korycansky, 2001), while at high ν one finds the horseshoe drag of an unperturbed disk profile (Masset, 2001).

Under most standard circumstances, the corotation torque can be safely neglected when evaluating an order of magnitude of the migration timescale in the linear regime. Indeed, even the fully unsaturated corotation torque amounts at most to a few tens of % of the differential Lindblad torque (Ward, 1997; Tanaka *et al.*, 2002), while Korycansky and Pollack (1993) found through numerical integrations that the corotation torque is an even smaller fraction of the differential Lindblad torque than given by analytical estimates.

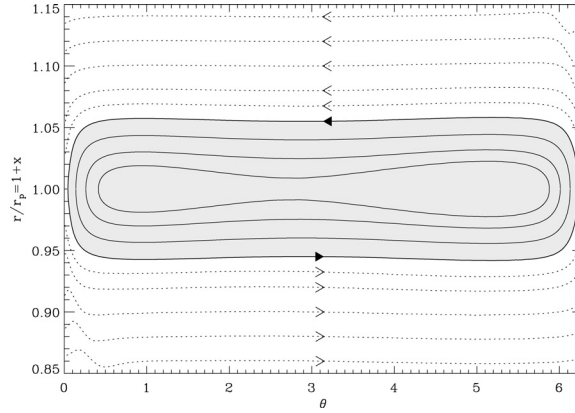


Fig. 14.3. Horseshoe region around the corotation of a planet in circular orbit (shaded area). The planet is located at $r = 1$ and $\theta = 0$ or 2π .

There are, however, noticeable exceptions for which neglecting the corotation torque can be misleading:

- A subgiant planet (typically Saturn sized) in a massive disk may result in runaway migration (also referred to as type III migration), based upon the action of the corotation torque, see Section 14.4.
- The corotation torque can also dominate over the differential Lindblad torque when a planet is located at a sharp surface-density gradient in a disk, such as the edge of a cavity.
- Finally, it seems that for Neptune-sized objects, the total torque estimate obtained from numerical simulations is much lower than the differential Lindblad torque (D'Angelo *et al.*, 2003a; Masset, 2002) and can even reverse migration if the disk is sufficiently thin (Masset, 2002), see Section 14.3.3. Additional work is required on the role of the corotation torque for this mass range, which could correspond to the onset of non-linear effects.

14.2.3 Type I migration-drift rate estimates

There is a number of estimates of the type I migration rate in the literature (see Ward, 1997 and refs. therein). The most recent linear calculations by Tanaka *et al.* (2002) take into account three-dimensional effects, and are based upon the value of the total tidal torque, including the corotation torque (fully unsaturated since it is a linear estimate). It reads (Tanaka *et al.*, 2002):

$$\tau \equiv a/\dot{a} = (2.7 + 1.1\alpha)^{-1} q^{-1} \frac{M_*}{\Sigma a^2} h^2 \Omega_p^{-1}, \quad (14.5)$$

for a surface-density profile $\Sigma \propto r^{-\alpha}$.

For an Earth-mass planet around a Solar-mass star at $r = 1$ AU, in a disk with $\Sigma = 1700 \text{ g cm}^{-2}$ and $h = 0.05$, this translates into $\tau = 1.6 \times 10^5$ years.

This analytical estimate has been verified by means of three-dimensional numerical simulations (Bate *et al.*, 2003b; D'Angelo *et al.*, 2003a). Both find an excellent agreement in the limit of low-mass, thus they essentially validate the linear analytical estimate. However, Bate *et al.* (2003b) and D'Angelo *et al.* (2003a) results differ for Neptune-sized objects. It is likely that non-linear effects begin to be important at this mass.

The type I migration timescale is very short, much shorter than the build up time of the $M_p \sim 5\text{--}15 M_\oplus$ solid core of a giant planet. Hence, type I migration constitutes a bottleneck for the accretion scenario for these massive cores. To date this remains an unsolved problem, but see the recent work by Alibert *et al.* (2004). Some recent attempts to include more detailed physics of the protoplanetary disk, such as opacity transitions and their impact on the disk profile (Menou and Goodman, 2004), or radiative transfer and the importance of shadowing in the planet vicinity (Jang-Condell and Sasselov, 2005), have lead to lower estimates of the type I migration rates which might help resolve the accretion/migration timescale discrepancy.

14.3 Type II migration

When the planet grows in mass it cannot be treated as a small perturbing object anymore. The gravitational interaction with the disk becomes non-linear and the wake of the planet turns into a shock. Eventually, for planetary masses around $1 M_J$ the density at the planetary orbit is lowered and an annular gap forms. In this regime numerical methods are used primarily to analyze the dynamical planet–disk interaction, the density structure of the disk, and the resulting gravitational torques acting on the planet. This non-linear regime is called type II migration.

14.3.1 Numerical modeling

The first modern high-resolution hydrodynamical calculations of planet–disk interaction were performed by Kley (1999), Bryden *et al.* (1999), and Lubow *et al.* (1999). Since protoplanetary accretion disks are assumed to be vertically thin, these first simulations used a two-dimensional ($r - \phi$) model of the accretion disk. The vertical thickness H of the disk was incorporated by assuming a given radial temperature profile $T(r) \propto r^{-1}$ which makes the ratio H/r constant. Typically the simulations assumed $H/r = 0.05$ which refers to a disk where at each radius the Keplerian speed is 20 times faster than the local sound speed. Initial density profiles typically had power laws for the surface density $\Sigma \propto r^{-s}$ with s between 0.5 and

1.5. Later also fully three-dimensional models were calculated which still use a simple isothermal equation of state today.

For the anomalous viscosity of accretion disks a Reynolds stress tensor formulation (Kley, 1999) is used typically where the kinematic viscosity ν is either constant or given by an α -prescription $\nu = \alpha c_s H$, where α is constant and c_s is the local sound speed. From observations, values lying between 10^{-4} and 10^{-2} are inferred for the α -parameter of protoplanetary disks. Full magnetohydrodynamic (MHD) calculations have shown that the viscous stress-tensor ansatz may give (for sufficiently long time averages) a reasonable approximation to the *mean* flow in a turbulent disk (Papaloizou and Nelson, 2003). The embedded planets are assumed to be point masses (using a smoothed potential), and together with the star they are treated as a classical N -body system. The disk also influences the orbits through gravitational torques. This is the desired effect to study as it will cause the orbital evolution of the planets. The planets may also accrete mass from the surrounding disk (Kley, 1999). To enhance resolution in the vicinity of the planet, the computations are typically performed in a rotating frame. Numerically, a special treatment of the Coriolis force has to be incorporated to ensure angular momentum conservation (Kley, 1998).

14.3.2 Viscous laminar Disks

The type of modeling outlined in the previous section yields, in general, smooth density and velocity profiles, and we refer to those models as *viscous laminar disk* models, in contrast to models which do not assume an a priori given viscosity and rather model the turbulent flow directly.

A typical result of such a viscous computation obtained with a 128×280 grid (in $r - \varphi$) is displayed in Fig. 14.4. Here, the planet with mass $M_p = 1 M_J$ and semi-major axis $a_p = 5.2$ AU is *not* allowed to move and remains on a fixed circular orbit, an approximation which is typical in many simulations. Clearly seen are the major effects an embedded planet has on the structure of the protoplanetary accretion disk. The gravitational force of the planet leads to a spiral wave pattern in the disk. In this calculation (Fig. 14.4) there are two spirals, in the outer disk and inner disks. The tightness of the spiral arms depends on the temperature (i.e. H/r) of the disk. The lower the temperature the tighter the spirals. The second prominent feature is the density gap at the location of the planet. It is caused by the deposition of positive (at larger radii) and negative (at smaller radii) angular momentum in the disk. The spiral waves are corotating in the frame of the planet, and hence their pattern speed is faster (outside) and slower (inside) than the disk material. Dissipation by shocks or viscosity leads to the deposition of angular momentum, and pushes material away from the planet. The equilibrium width of the gap is determined by

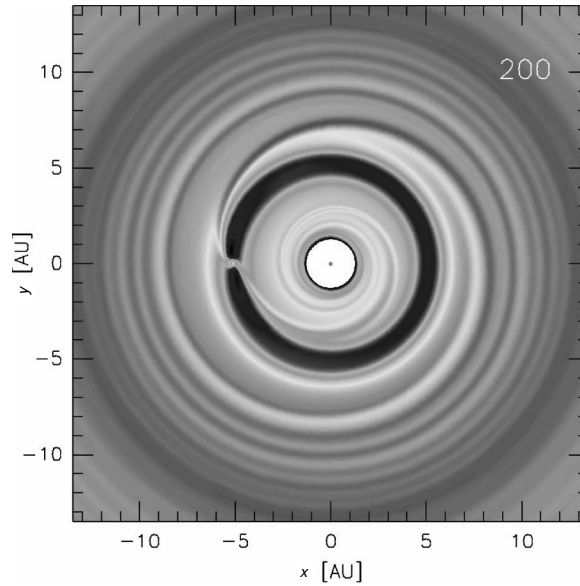


Fig. 14.4. Surface-density profile for an initially axisymmetric planet–disk model after 200 orbits of the planet.

the balance of gap-closing viscous and pressure forces and gap-opening gravitational torques. For typical parameters of a protoplanetary disk, a Saturn-mass planet will begin to open a visible gap. More details on gap-opening criteria are given in the review by Lin and Papaloizou (1993), and see also Bryden *et al.* (1999).

To obtain more insight into the flow near the planet and to calculate accurately the torques of the disk acting on the planet, a much higher spatial resolution is required. As this is necessary only in the immediate surroundings of the planet, a number of nested-grid and also variable grid-size simulations have been performed (D’Angelo *et al.*, 2002, 2003a; Bate *et al.*, 2003b). Such a grid system is not adaptive, as it is defined at the beginning of the computation and does not change with time. The planet is placed in the center of the finest grid.

The result for a two-dimensional computation using six grids is displayed in Fig. 14.5, for more details see also D’Angelo *et al.* (2002). The top left base grid has a resolution of 128×440 and each sub-grid has a size of 64×64 with a refinement factor of two from level to level. It is noticeable that the spiral arms inside the Roche-lobe of the planet are detached from the global outer spirals. The two-armed spiral around the planet extends deep inside the Roche-lobe and allows for the accretion of material onto the planet. The nested-grid calculations have recently been extended to three dimensions and a whole range of planetary masses have been investigated, starting from $1 M_{\oplus}$ to a few M_J (Kley *et al.*, 2001; D’Angelo *et al.*, 2003a). In the three-dimensional case the strength of the spiral

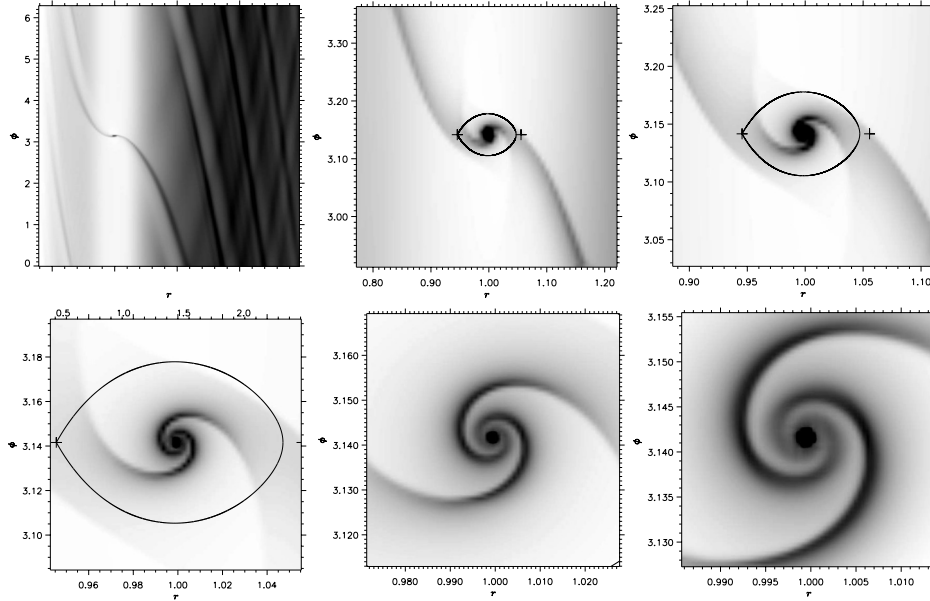


Fig. 14.5. Density structure of a $1 M_J$ planet on each level of the nested grid system, consisting of six grid levels in total. The top left panel displays the total computational domain. The line indicates the size of the Roche lobe.

arms is weaker and accretion occurs primarily from regions above and below the midplane of the disk.

14.3.3 The migration rate

Such high-resolution numerical computations allow for a detailed computation of the torque exerted by the disk material onto the planet, and its mass-accretion rates. Figure 14.6 gives the inverse $1/\tau_M$ of the migration for three-dimensional nested-grid calculations as a function of the planet mass, given in units of the mass of the central star, $q = M_p/M_\odot$. The straight line by Tanaka *et al.* (2002) assumes a three-dimensional flow and takes the corotation torques into account. The symbols refer to different approximations of the potential of the planet. It can be seen that for low masses $q \approx 10^{-5}$ and intermediate masses $q \approx 8 \times 10^{-5}$ the numerical results fit well to the linear theory. In the intermediate range of about $q \approx 3 \times 10^{-5}$ the migration rates are about an order of magnitude smaller (D'Angelo *et al.*, 2003a). This effect may be caused by the onset of gap formation in the mass range of about $10\text{--}15 M_\oplus$. Here non-linear effects begin to set in and modify the physics. These results should be compared to those obtained by Bate *et al.* (2003b) and Masset (2002).

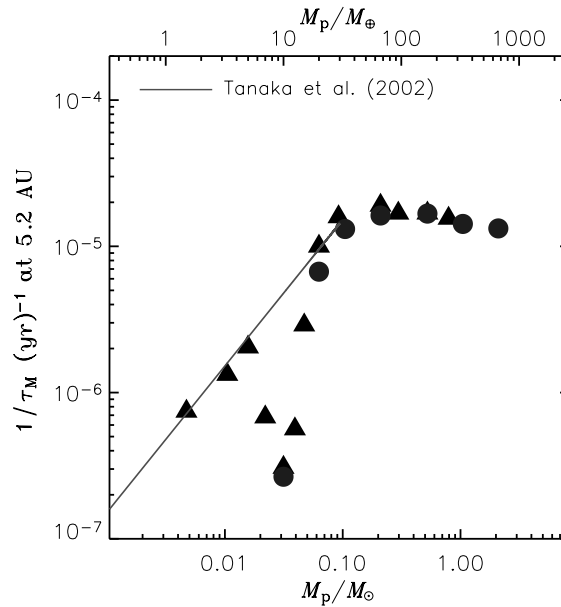


Fig. 14.6. The inverse migration rate for different planet masses. The symbols denote different approximations (smoothing) for the potential of the planet. The solid line refers to linear results for Type I migration from Tanaka *et al.* (2002).

The consequences of accretion and migration have been studied by numerical computations which do not hold the planet fixed at some radius but rather follow the orbital evolution of the planet (Nelson *et al.*, 2000), allowing planetary growth. The typical migration and accretion timescales are of the order of 10^5 yr, while the accretion timescale may be slightly smaller. This is in very good agreement with the estimates obtained from the models using a fixed planet. These simulations show that during their inward migration they grow up to about $4 M_J$.

The consequence of the inclusion of thermodynamic effects (viscous heating and radiative cooling) has been studied by D'Angelo *et al.* (2003b) in two-dimensional calculations, where an increased temperature in the circumplanetary disk has been found. This has interesting consequences for the possible detection of an embedded protoplanet (Wolf *et al.*, 2002). The effect that the self-gravity of the disk has on migration has been analyzed through numerical simulations (Nelson and Benz, 2003a,b). For typical disk masses the influence is rather small.

14.3.4 Inviscid disks

To investigate the influence of viscosity we also studied recently inviscid models with no physical viscosity added. Only a numerical bulk viscosity has to be added

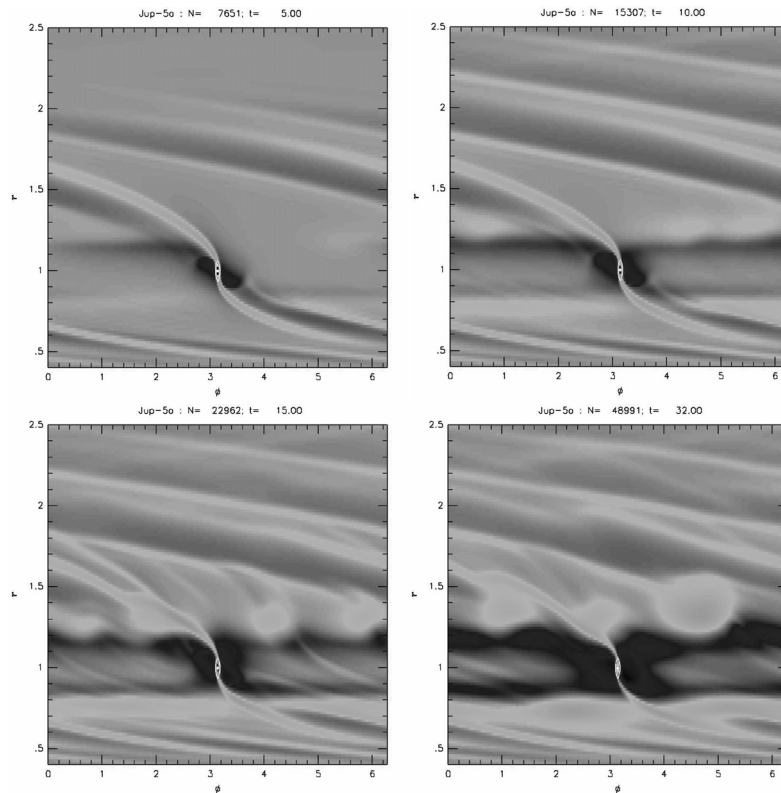


Fig. 14.7. Results of an inviscid disk computation with an embedded $1 M_J$ planet. Results are displayed at four different times (5, 10, 15, and 32) in units of the orbital period of the planet. Shown are gray-scale plots of the surface density in an $(r - \varphi)$ -coordinate system.

to ensure numerical stability (Kley, 1999). However, this has no influence on the physical effects of the simulations. In Fig. 14.7 we display the density structure of such an inviscid model for a $1 M_J$ planet. The planet is not allowed to move and for stability purposes its mass is gradually switched on during the first five orbits. Results are displayed at four different times (5, 10, 15, 32). After only five orbits the spiral waves are already clearly visible, as they form on a dynamical timescale. The gap is just beginning to clear. At the edges of the gap high density blobs (*vortices*) are forming which are reduced in number through merging. Eventually only one big blob remains. Also inside the gap, some detailed structure is visible. In comparison, fully viscous simulations show these vortices mostly as transient features at the beginning of the simulations. They vanish later on as a result of the viscosity. Vortices in a inviscid disk with an embedded planet have also been studied by Koller *et al.* (2003).

If accretion and also migration of the planet is considered, these moving vortices may create some more complex time dependence. However, the details of such inviscid models will have to be studied in future work. Vortices in accretion disks have sometimes been considered to enhance planet formation either through triggering a direct gravitational instability or by trapping particles in it (Goden and Livio, 2000; de la Fuente Marcos and Barge, 2001; Klahr and Bodenheimer, 2003).

14.4 Type III migration

Thus far, the torque acting on a migrating planet was considered to be independent of its migration rate. This is true for the differential Lindblad torque. However, the corotation torque implies material that crosses the planet orbit on the U-turn of the horseshoe, streamlines. In a non-migrating case, only the trapped material of the horseshoe region participates in these U-turns, but in the case of an inwards (resp. outwards) migrating planet, material of the inner disk (resp. outer disk) has to flow across the co-orbital region and executes one horseshoe U-turn to do so. By doing this, it exerts a corotation torque on the planet that scales with the drift rate. We give below a simplified derivation of the corotation torque dependency upon the drift rate \dot{a} . A more accurate derivation can be found in Masset and Papaloizou (2003).

We will call x_s the half radial width of the horseshoe region. The amount of specific angular momentum that a fluid element near the separatrix takes from the planet when it switches from an orbit with radius $a - x_s$ to $a + x_s$ is $4Bax_s$.

The torque exerted on the planet in steady migration with drift rate \dot{a} by the inner or outer disk elements as they cross the planet orbit on a horseshoe U-turn is therefore, to the lowest order in x_s/a ,

$$\Gamma_2 = (2\pi a \Sigma_s \dot{a}) \cdot (4Bax_s), \quad (14.6)$$

where we keep the same notation as in Masset and Papaloizou (2003), and where Σ_s is the surface density at the upstream separatrix. The first bracket in the above equation represents the mass flow rate from the inner disk to the outer one (or vice versa, depending on the sign of \dot{a}). As the system of interest for which we evaluate the sum of external torques, we take the system composed of the planet and all fluid elements trapped in libration in its co-orbital region, namely the whole horseshoe region (with mass M_{HS}) and the Roche lobe content (with mass M_R), because all of these parts perform a simultaneous migration.

The drift rate of this system is then given by

$$(M_p + M_{HS} + M_R) \cdot (2Ba\dot{a}) = (4\pi ax_s \Sigma_s) \cdot (2Ba\dot{a}) + \Gamma_{LR}, \quad (14.7)$$

which can be rewritten as

$$m_p \cdot (2Ba\dot{a}) = (4\pi a \Sigma_s x_s - M_{\text{HS}}) \cdot (2Ba\dot{a}) + \Gamma_{\text{LR}}, \quad (14.8)$$

where $m_p = M_p + M_R$ is the mass content of the Roche lobe, including the planet, which for short we also refer to as the planet mass, assuming that the material orbiting the circumplanetary disk “belongs” to the planet. The first term of the first bracket of the r.h.s. corresponds to the horseshoe region surface multiplied by the upstream separatrix surface density, hence it is the mass that the horseshoe region would have if it had a uniform surface density equal to the upstream surface density. The second term is the actual horseshoe region mass. The difference between these two terms is called, in Masset and Papaloizou (2003), the coorbital mass deficit and denoted δm . Note that we could also have included the Roche lobe mass in the coorbital mass deficit and kept the planet mass as the mass of the point-like object at the center of the Roche lobe alone. This choice would lead to an equivalent formulation, and to the same runaway criterion. Equation (14.8) yields a drift rate

$$\dot{a} = \frac{\Gamma_{\text{LR}}}{2Ba(m_p - \delta m)}. \quad (14.9)$$

This drift rate is faster than the standard estimate in which one neglects δm . This comes from the fact that the co-orbital dynamics alleviates the differential Lindblad torque task by displacing fluid elements from the upstream to the downstream separatrix. The angular momentum they extract from the planet by doing so favors its migration.

As δm tends to m_p , most of the angular momentum lost by the planet and its co-orbital region is gained by the orbit-crossing circulating material, making migration increasingly cost effective.

When $\delta m \geq m_p$, the above analysis, assuming a steady migration (\dot{a} constant), is no longer valid. Migration undergoes a runaway, and has a strongly time-varying migration rate, that increases exponentially over the first libration timescales. An analysis similar to the above calculation may be performed, in which the corotation torque depends on the migration rate, except that one now has to introduce a delay τ between the mass inflow at the upstream separatrix and its consequence on the corotation torque. This delay represents the feedback loop latency,

$$\Gamma_{\text{CR}}(t) = 2Ba\delta m\dot{a}(t - \tau). \quad (14.10)$$

A Taylor expansion in time of $\dot{a}(t - \tau)$ yields a first order differential equation for \dot{a} (Masset and Papaloizou, 2003). The linear dependence of the corotation on the drift rate remains valid as long as the semi-major-axis variation over a horseshoe

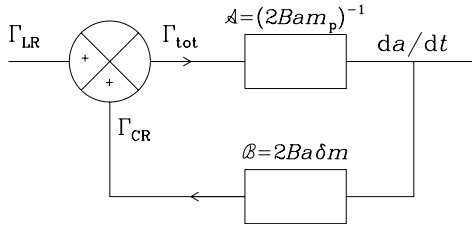


Fig. 14.8. Schematic representation of the positive feedback loop. The loop latency is $\sim \tau_{\text{lib}}$.

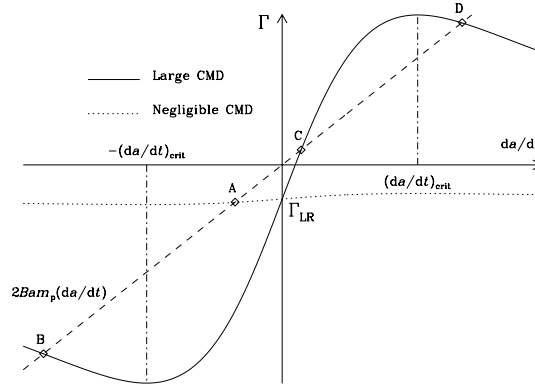


Fig. 14.9. The solid curve shows the total torque on the planet in a massive disk (hence with a large co-orbital mass deficit) as a function of the drift rate. For $|\dot{a}| \ll \dot{a}_{\text{crit}}$ the torque exhibits a linear dependence in \dot{a} . The dotted line shows the torque in a low mass disk (i.e. with a negligible co-orbital mass deficit), in which case the torque is almost independent of the migration rate and is always close to the differential Lindblad torque Γ_{LR} . The dashed line represents the planet angular-momentum-gain rate as a function of \dot{a} , assuming a circular orbit. For a given situation, the migration rate achieved by the planet is given by the intersection of the dashed line with the torque curve. In the low-mass disk case, the intersection point, A, is unique, and stable. It yields a negative drift rate controlled by the differential Lindblad torque. In the high-mass disk case (runaway case), there are three points of intersection (B, C and D). The central point (C) is unstable, while the extreme ones (B and D) are stable and correspond to the maximum runaway drift attained by the planet, either inwards (point B) or outwards (point D).

libration time is smaller than the horseshoe zone width, i.e.

$$|\dot{a}| < \dot{a}_{\text{crit}} = \frac{Ax_s^2}{2\pi a}. \quad (14.11)$$

The corotation torque then reaches a maximum and slowly decays for larger values of \dot{a} (see Fig. 14.9).

We should comment that the mechanism upon which type III (or runaway) migration is based can be described by the standard formalism of positive feedback loops, as shown in Fig. 14.8.

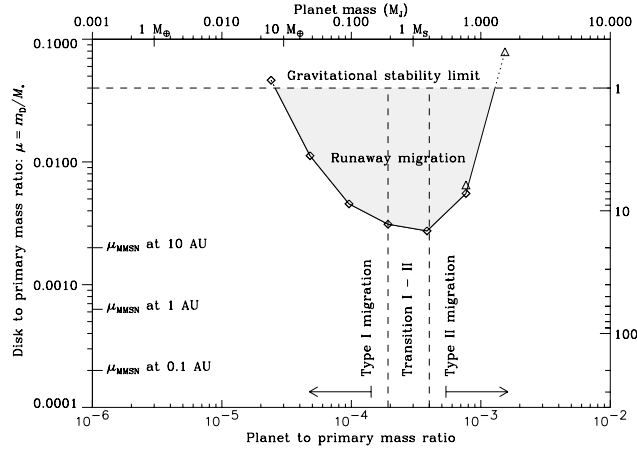


Fig. 14.10. Runaway-limit domain for a $H/r = 0.04$ and $\nu = 10^{-5}$ disk, with a surface density profile $\Sigma \propto r^{-3/2}$. The variable $m_D = \pi \Sigma r^2$ features on the y axis. It is meant to represent the local disk mass, and it therefore depends on the radius. Runaway is most likely for Saturn-mass planets. These would undergo runaway in disks no more massive than a few times the minimum-mass Solar Nebula. Runaway is impossible for massive planets ($M > 1 M_J$) as the surface density is very low at the upstream separatrix. Low mass objects ($M < 10 M_\oplus$) do not deplete their co-orbital region and therefore cannot undergo a runaway.

The open loop gain is $G' = \mathcal{A}\mathcal{B} = \delta m/m_p$, so the system stability condition, which is $G' < 1$ reads here $\delta m < m_p$. Above this threshold, one gets a runaway. Below, the closed loop gain, which is given by

$$G = \frac{\mathcal{A}}{1 - \mathcal{A}\mathcal{B}}, \quad (14.12)$$

yields Equation (14.9).

A standard bifurcation analysis can be performed on this feedback loop, as illustrated in Fig. 14.9. The transition from one case to the other (one intersection point to three intersection points) occurs when the angular-momentum-change rate line (which has slope $2Bam_p$) and the torque curve near the origin are parallel. Since this latter has a slope $2Ba\delta m$ near the origin, the transition occurs for $m_p = \delta m$.

The disk critical mass above which a planet of given mass undergoes a runaway depends on the disk parameters (aspect ratio and effective viscosity). The limit has been worked out by Masset and Papaloizou (2003) for different disk aspect ratios and a kinematic viscosity $\nu = 10^{-5}$. We reproduce in Fig. 14.10 the type III-migration domain for a disk with $H/r = 0.04$.

14.5 Other modes of migration

We shall briefly mention another mode of migration recently studied by Nelson and Papaloizou (2004), Laughlin *et al.* (2004) and Nelson (2005), which deals with the evolution of small-mass objects (those which would undergo type I migration in a laminar disk) embedded in disks invaded by magnetorotational turbulence. The torque of the disk acting on the planet is then a strongly time-varying quantity, which endows the planet with a random walk motion in the semimajor axis, rather than yielding the monotonous decrease observed in type I migration. This random walk motion, sometimes referred to as “diffusive” or “stochastic” migration, involves even very low-mass objects, which would undergo a negligible migration in laminar disks. Also, as superimposed onto the global drift under the wake action, it exacerbates the problem of type I migration in the sense that it lowers the timescale expectancy for a given protoplanet to reach the central object, but, being probabilistic in nature, it also seems to leave room for a small fraction of objects which never reach the central object over the turbulent-disk lifetime. A more conclusive outcome would require computations that are currently not possible. The interested reader should refer to the above references for further details.

14.6 Eccentricity driving

The population of extrasolar giant planets with orbital periods larger than ten days displays an important scatter in eccentricity, which can reach, for some systems, values as large as 0.9. Thus far the origin of these eccentricities has not been elucidated. Planet–planet interactions (Ford *et al.*, 2001) and disk–planet interactions (Goldreich and Sari, 2003) have been proposed to be responsible for the excitation of giant-planet eccentricities. Here we sum up the basics of the driving of eccentricity through disk–planet resonant interactions, and we comment on recent developments on this subject.

In Section 14.2 we outlined the angular-momentum exchange between a planet on a circular orbit and the disk at the principal Lindblad resonances and at the co-orbital corotation resonances. A planet on an eccentric orbit interacts with the disk at additional resonances. Indeed, in addition to the potential components with pattern frequency Ω_p (see Equation 14.1), other potential components appear with pattern frequencies $\Omega_p + \frac{k}{m}\kappa_p$, and with amplitudes scaling as $e^{|k|}$. Assuming that the eccentricity is low, one can restrict the analysis to the terms that scale with e . The resonances associated with these terms are called respectively the first-order Lindblad and corotation resonances. While the principal Lindblad resonances negligibly contribute to the eccentricity driving or damping, the first-order Lindblad resonances can lead to substantial eccentricity variation over a timescale much smaller than the migration timescale. Specifically, the first-order Lindblad

resonances can be divided into two groups: the coorbital Lindblad resonances, which damp the eccentricity, and the external Lindblad resonances, which excite the eccentricity. In the case of a giant protoplanet that opens a clean gap, the coorbital Lindblad resonances fall in the middle of the gap and are “switched off”, hence as a net result the first-order Lindblad resonances excite the eccentricity. In addition, it can be shown that the first-order corotation resonances damp the eccentricity. The damping timescale can be directly compared to the excitation timescale by the first-order Lindblad resonances (Goldreich and Tremaine, 1980). One finds that eccentricity damping dominates by a small margin of $\sim 5\%$. This would be the end of the story if corotation resonances did not saturate. However, if for a given planet eccentricity, the disk viscosity is low enough, the corotation resonances can be sufficiently saturated to reverse the eccentricity balance. The analyses of Ogilvie and Lubow (2003) and Goldreich and Sari (2003), which assume a perfectly clean gap (i.e. no damping by the co-orbital Lindblad resonances), suggest that a Jupiter-sized protoplanet embedded in a disk with $H/r = 4\text{--}5\%$ and a viscosity $\alpha \sim 10^{-3}$ can undergo an eccentricity excitation if its initial eccentricity is as low as 0.01. These analytical works rely upon simplifying assumptions, as they consider the saturation of isolated corotation resonances, therefore neglecting the overlap between successive corotation resonances. They also neglect the fact that the first-order corotation resonances share their location with the principal Lindblad resonances. However, a numerical study of the two-resonance case (either corotation-corotation or corotation-Lindblad) show that the saturation properties of a non-isolated corotation resonance are very similar to the properties of an isolated one (Masset and Ogilvie, 2004). This seems to indicate that the above analytical studies essentially provide a correct evaluation of the saturation of the first-order corotation resonances. Nevertheless, no eccentricity excitation for planetary-mass objects has ever been observed in numerical simulations of disk–planet interactions (Papaloizou *et al.*, 2001). This could be a mesh-resolution effect (Masset and Ogilvie, 2004), but more recent simulations performed at higher resolution do not exhibit eccentricity excitation either. One explanation is that the gap opened by a Jupiter-sized planet in a disk such as the one mentioned above, is far from being clean, so that co-orbital Lindblad resonances still sizably contribute to eccentricity damping. Another issue that needs to be properly dealt with by numerical simulations is the secular exchange of eccentricity between the planet and the disk (see Masset and Ogilvie, 2004 and refs. therein). This exchange occurs on extremely long timescales ($\gg 10^3$ orbits), which constitute a challenge for hydrodynamic numerical simulations of disk–planet interactions.